PNAS RESEARCH ARTICLE | BIOCHEMISTRY OPEN ACCESS

Structure of the human respiratory complex II

Zhanqiang Du[a,1], Xiaoting Zhou[b,1], Yuezheng Lai[a], Jinxu Xu[a], Yuying Zhang[a], Shan Zhou[a], Ziyan Feng[a], Long Yu[a], Yanting Tang[a], Weiwei Wang[c], Lu Yu[d], Changlin Tian[d], Ting Ran[e], Hongming Chen[e], Luke W. Guddat[f], Fengjiang Liu[e,2], Yan Gao[c,2], Zihe Rao[a,c,f,g,h,2], and Hongri Gong[a,2]

Edited by Dinshaw Patel, Memorial Sloan Kettering Cancer Center, New York, NY; received September 29, 2022; accepted March 10, 2023

Human complex II is a key protein complex that links two essential energy-producing processes: the tricarboxylic acid cycle and oxidative phosphorylation. Deficiencies due to mutagenesis have been shown to cause mitochondrial disease and some types of cancers. However, the structure of this complex is yet to be resolved, hindering a comprehensive understanding of the functional aspects of this molecular machine. Here, we have determined the structure of human complex II in the presence of ubiquinone at 2.86 Å resolution by cryoelectron microscopy, showing it comprises two water-soluble subunits, SDHA and SDHB, and two membrane-spanning subunits, SDHC and SDHD. This structure allows us to propose a route for electron transfer. In addition, clinically relevant mutations are mapped onto the structure. This mapping provides a molecular understanding to explain why these variants have the potential to produce disease.

electron transport chain | human complex II | cryoelectron microscopy

Significance

Human complex II deficiency resulting from mutations in the structural subunit genes can lead to metabolic disease or cancer. Here, we have determined the structure of this complex which explains how it effectively transports electrons but also explains why mutations to this complex lead to disease. The study lays a foundation for the development of therapeutic approaches to treat these maladies.

The mitochondrial oxidative phosphorylation (OXPHOS) system is central to cellular metabolism during aerobic respiration in eukaryotic cells (1, 2). It comprises five enzymatic complexes (complexes I-V, CI-CV) along with two mobile electron carriers (ubiquinone and cytochrome *c*) and is located in the inner mitochondrial membrane. The respiratory chain (also called electron transport chain) consists of complexes I-IV. It oxidizes the reducing equivalents in nicotinamide adenine dinucleotide (NADH) and succinate using molecular oxygen and couples the translocation of protons from the mitochondrial matrix into the intermembrane space. This process drives the production of adenosine triphosphatase (ATP) by F_1F_o-ATP synthase (complex V).

Respiratory complex II plays a crucial role in the two primary key metabolic pathways for generating ATP: the Krebs cycle (also known as tricarboxylic acid, TCA) and the OXPHOS pathway (3). It can function in either aerobic energy metabolism [termed succinate-ubiquinone reductase (SQR) or succinate dehydrogenase (SDH)] or anaerobic energy metabolism [termed quinol-fumarate reductase (QFR) or fumarate reductase (FRD)] in the mammalian mitochondria (3, 4). Human respiratory complex II (CII) is the source of a broad range of human diseases related to its malfunction. These include several types of cancers (5, 6) and neurodegenerative disorders (7). Thus, understanding how human CII operates can support the development of therapeutic approaches to treat these diseases. To date, the complete structures of complex II from *Wolinella succinogenes* (8), *Escherichia coli* (9, 10), *Sus scrofa* (11), *Gallus gallus* (12), *Ascaris suum* (13), and *Mycobacterium smegmatis* (14, 15) have been determined. Remarkably, although the structural and mechanistic properties of CII from these species have been studied extensively, little is known about the structure and machinery of human CII. Here, we report the cryoelectron microscopy (cryo-EM) structure of this complex, which advances our understanding of how it transports electrons, as well as giving insights into the molecular basis for diseases associated with its defects.

Results and Discussion

Purification and Characterization of Human CII. To isolate human CII, a 3× Flag tag was incorporated at the C terminus of the SDHD subunit. This construct was then inserted into an expression plasmid, which was then transferred into human embryonic kidney (HEK) 293F cells (*SI Appendix*, Fig. S1*A*). FLAG affinity chromatography and gel filtration column were then performed to obtain a supramolecular assembly (*SI Appendix*, Fig. S1*B*). A single band was shown on blue native polyacrylamide gel electrophoresis (BN-PAGE), which indicated that human CII is present (*SI Appendix*, Fig. S1*C*). All the four subunits (SDHA, SDHB, SDHC, and SDHD) were detected by SDS-PAGE (*SI Appendix*, Fig. S1*D*) and mass spectrometry (MS) (*SI Appendix*, Table S1). Electron paramagnetic resonance (EPR) spectra revealed the presence of redox centers, containing the [2Fe-2S] cluster, the [4Fe-4S] cluster, the [3Fe-4S] cluster, and one *b*-type heme group (*SI Appendix*, Fig. S1*E*). Human CII coupled succinate oxidation to ubiquinone reduction gave a

Author affiliations: [a]State Key Laboratory of Medicinal Chemical Biology, Frontiers Science Center for Cell Responses, College of Life Sciences, Nankai University, Tianjin 300353, China; [b]State Key Laboratory of Reproductive Regulation and Breeding of Grassland Livestock, School of Life Sciences, Inner Mongolia University, Hohhot 010070, China; [c]Shanghai Institute for Advanced Immunochemical Studies and School of Life Science and Technology, ShanghaiTech University, Shanghai 201210, China.; [d]High Magnetic Field Laboratory, Chinese Academy of Sciences, Hefei 230031, China; [e]Innovative Center For Pathogen Research, Guangzhou Laboratory, Guangzhou 510005, China; [f]School of Chemistry and Molecular Biosciences, The University of Queensland, Brisbane, QLD 4072, Australia; [g]National Laboratory of Biomacromolecules, CAS Center for Excellence in Biomacromolecules, Institute of Biophysics, Chinese Academy of Sciences, Beijing 100101, China; and [h]Laboratory of Structural Biology, Tsinghua University, Beijing 100084, China

Author contributions: Z.R. and H.G. designed research; Z.D., X.Z., T.R., H.C., F.L., and Y.G. performed research; Z.D., X.Z., Y.L., J.X., Y.Z., S.Z., Z.F., L.Y., Y.T., W.W., L.Y., C.T., L.G., F.L., Y.G., and H.G. analyzed data; and Z.D., X.Z., L.G., and H.G. wrote the paper.

The authors declare no competing interest.

This article is a PNAS Direct Submission.

[1]Z.D. and X.Z. contributed equally to this work.

[2]To whom correspondence may be addressed. Email: liu_fengjiang@gzlab.ac.cn, gaoyan@shanghaitech.edu.cn, raozh@tsinghua.edu.cn, or gonghr@nankai.edu.cn.

This article contains supporting information online at https://www.pnas.org/lookup/suppl/doi:10.1073/pnas.2216713120/-/DCSupplemental.

Published April 25, 2023.

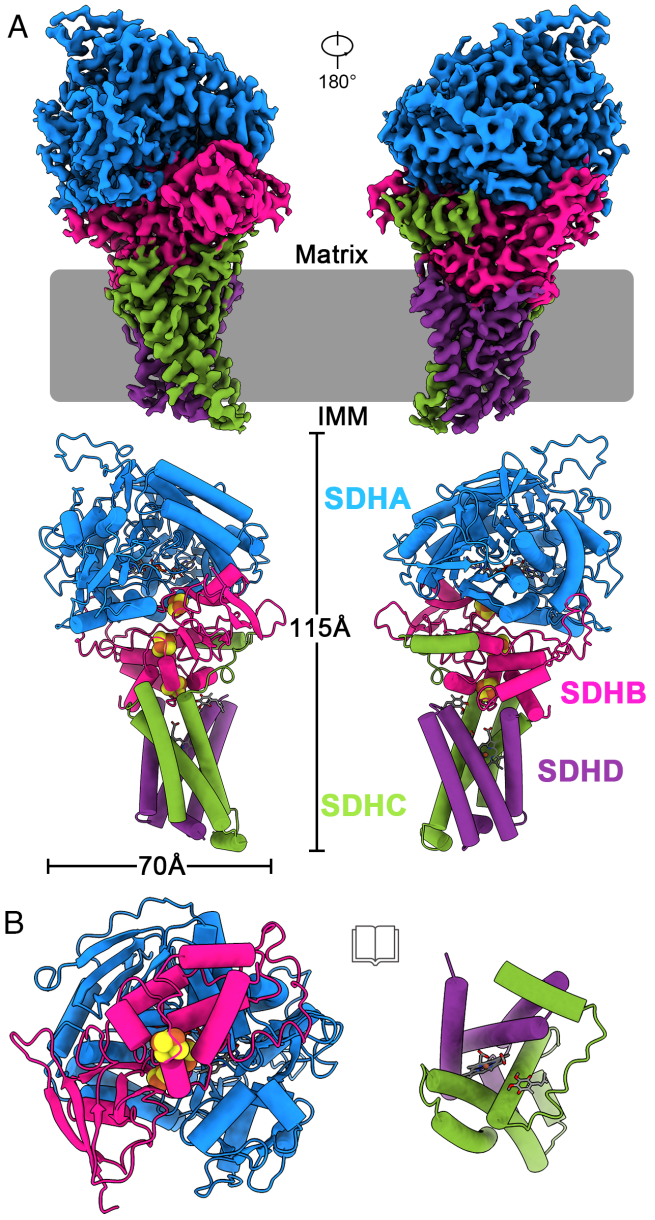

Fig. 1. Structure of human respiratory complex II. (*A*) Single-particle cryo-EM density map of human CII at 2.86 Å resolution. Two views are shown: the front view (*Left*) and the back view (*Right*). Structure of the human CII atomic model from the same views is shown in cartoon representation. SDHA, SDHB, SDHC, and SDHD are colored in blue, pink, green, and purple, respectively. The complex has approximate dimensions of 115 by 70 Å (height and width). (*B*) The soluble region (SDHA and SDHB subunits) and transmembrane anchor region (SDHC and SDHD subunits) are shown in cartoon representation and indicated in an open-book configuration. IMM, inner mitochondrial membrane.

catalytic constant (k_{cat}) 0.67 ± 0.02 s^{-1} (*SI Appendix*, Table S2), confirming that the purified human CII is a functioning complex.

Structure of the Human CII. The structure of human CII was determined by cryo-EM to an overall resolution of 2.86 Å (*SI Appendix*, Figs. S2 and S3 and Tables S3 and S4). We observed all four subunits in a monomeric assembly (Fig. 1*A*). This arrangement is similar to that in *W. succinogenes* QFR (8), *E. coli* QFR (9), *S. scrofa* SQR (11), and *M. smegmatis* SQR (15) with human CII also adopting a mushroom-like shape with a hydrophilic head and a hydrophobic transmembrane-anchored tail (Fig. 1*A*). The hydrophilic head of human CII consists of the flavin adenine dinucleotide (FAD)–binding protein (SDHA) and the iron–sulfur protein (SDHB) (Fig. 1*B*). The entire hydrophobic domain contains two membrane-anchored subunits: SDHC and SDHD (Fig. 1*B*). The SDHA subunit can be divided into four domains (11) termed the FAD-binding domain, capping domain, helical domain, and C-terminal domain (Fig. 2*A*). The active site for succinate–fumarate interconversion is located at the interface between the FAD-binding domain and the capping domain. SDHB is a small iron–sulfur protein harboring a [2Fe-2S], a [4Fe-4S], and a [3Fe-4S] cluster and organized into two domains in a butterfly-like shape (Fig. 2*B*). The [2Fe-2S] cluster is coordinated by a loop located in the N-terminal domain, and the [4Fe-4S] and [3Fe-4S] clusters are assembled on the C-terminal domain (Fig. 2*B*). Overall, these soluble domains (SDHA and SDHB) are similar in fold to the previously reported bacterial and mitochondrial respiratory CIIs (8–15) (*SI Appendix*, Fig. S4). In contrast, the structures and components of the integral membrane domain of CIIs can vary containing 1, 2, or 3 membrane-bound subunits, possess varying prosthetic groups (heme *b* or Fe-S cluster), and even have different numbers of heme *b* groups (0, 1, or 2) (8–15). The two membrane-anchored proteins (SDHC and SDHD) in human CII, each with three transmembrane helices, contain only one heme *b* group. The transmembrane helices of SDHC and SDHD exhibit a similar fold to each other (Fig. 2*C*). Notably, the structural features of the membrane domain of human CII are also most similar to that of the *E. coli* (10) and *S. scrofa* (11) SQRs (*SI Appendix*, Fig. S4).

Density for a phosphatidylethanolamine (PE) unit is observed (*SI Appendix*, Fig. S3) and positioned at the interface on the mitochondrial inner membrane side between SDHC and SDHD and located directly below the heme *b* group (Fig. 2*C*). PE is also observed in *S. scrofa* SQR (11) (*SI Appendix*, Fig. S5*A*). However, in *E. coli* SQR (10), the position equivalent to the PE site is occupied by a cardiolipin (CDL) molecule, and in the *W. succinogenes* QFR (8) and *M. smegmatis* Sdh2 (14) (*SI Appendix*, Fig. S5*A*), the position equivalent to the PE site is occupied by a heme *b*. Structure determination of membrane proteins has highlighted the many roles played by lipid molecules in influencing overall structural and functional integrity (16). It has been shown that PE lipids play a role in stabilizing the inward conformation of *E. coli* xylose transporter XylE and lactose permease LacY (17), maintaining the structural stability of the *E. coli* ABC transporter McjD by providing the correct hydrophobic environment (18) and facilitating the functional dimer formation of *Aspergillus nidulans* purine transporter UapA (19). CDL was observed to stabilize and facilitate the assembly of the *E. coli* Na^+/H^+ antiporter NhaA (20). In the present study, we used molecular dynamics (MD) simulations to understand how PE binding and dissociation events regulate the conformational stability of human CII at the molecular level. The results of the MD simulations suggest that the PE molecule here is also linked to protein stability (*SI Appendix*, Fig. S5*B*). In addition, the heme cofactor is also crucial for the heme protein to achieve its proper fold and thus become a stable, functional structure (21). Taken together, the ligand in human CII and its counterparts in other organisms are believed to play crucial roles by modulating the conformational, structural, and functional properties of the protein, and its heterogeneity may be related to species specificity.

Electron Transfer Pathway in the Human CII. The prosthetic groups (FAD, [2Fe-2S], [4Fe-4S], [3Fe-4S], and a *b*-type heme groups) mediating the electron transfer were all unambiguously assigned into the cryo-EM map (*SI Appendix*, Fig. S3). The edge-to-edge distance between these redox-active prosthetic groups is less than 14 Å (Fig. 3), a distance range that can efficiently support

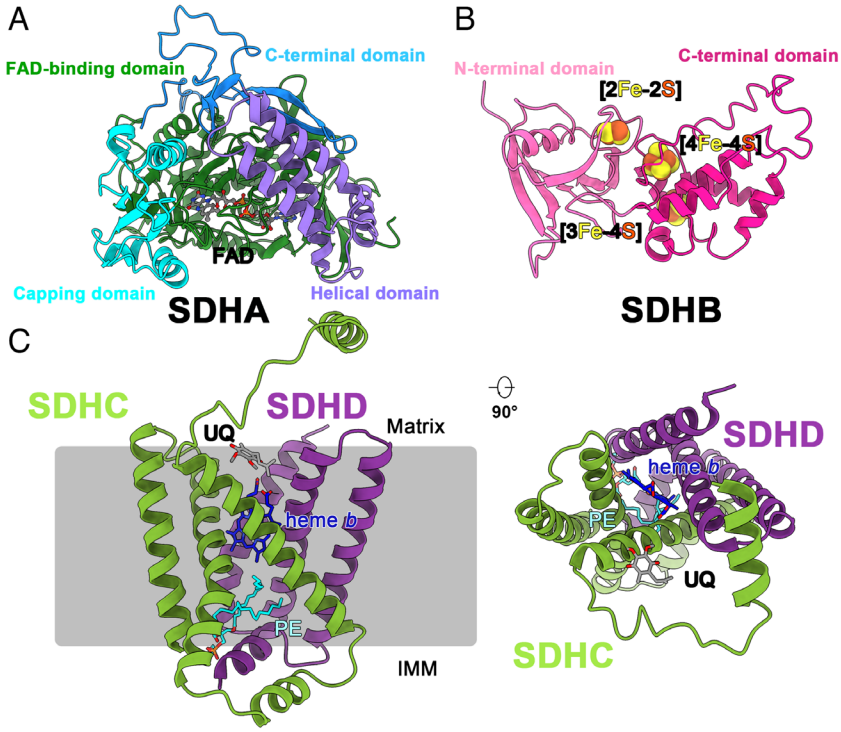

Fig. 2. Composition of human CII. (*A*) SDHA consists of four subdomains: the FAD-binding domain (residues A51 to A315 and A403 to A487), the capping domain (residues A316 to A402), the helical domain (residues A488 to A585), and the C-terminal domain (residues A596 to A664). FAD is presented as a stick model. (*B*) SDHB contains two domains: the N-terminal domain (residues A35 to A142) and the C-terminal domain (residues A143 to A273). Three FeS clusters are shown in sphere representation. (*C*) Two integral membrane domains of SDHC and SDHD are shown in two orthogonal views. Ubiquinone (UQ), phosphatidylethanolamine (PE), and heme *b* are shown as stick models. IMM, inner mitochondrial membrane.

the delivery of electrons between these redox centers (22). The EPR signal (g = 2.0) indicates the presence of ubiquinone (UQ) (*SI Appendix*, Fig. S1*E*). UQ is also observed to bind at the entrance of the pocket formed by the transmembrane helix I of SDHC, transmembrane helix II of SDHD, and the C-terminal segment of SDHB. It interacts with Pro-SDHB197, Trp-SDHB201,

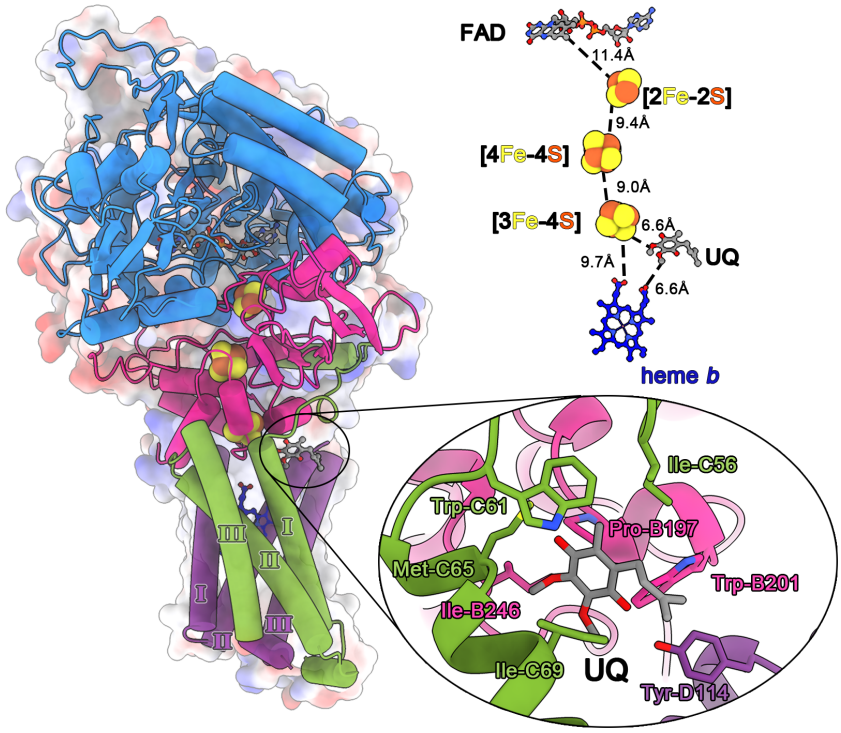

Fig. 3. Prosthetic groups in human CII and the pathway of electron transfer. (*Left*) Overall structure of human CII is shown together with the prosthetic groups. A zoomed-in view of UQ-binding site representation indicates the interactions between the UQ and surrounding residues. (*Right*) Prosthetic groups in the path of electron transfer are labeled with edge-to-edge distances. Five prosthetic groups, FAD, [2Fe-2S], [4Fe-4S], [3Fe-4S], and a heme *b* are required for electron transfer flow from succinate to ubiquinone. Prosthetic groups are shown in stick models or as spheres. The transmembrane helices are labeled.

Ile-SDHB246, Ile-SDHC56, Trp-SDHC61, Met-SDHC65, Ile-SDHC69, and Tyr-SDHD114 (Fig. 3). The edge-to-edge distances between UQ and heme *b* and [3Fe-4S] are about 6.6 Å and 6.6 Å, respectively, which are efficient to promote electron transfer (22).

In *E. coli* (10) and *S. scrofa* (11) SQRs, the electrons released from succinate oxidation are transferred to the [3Fe-4S] by sequential delivery through a chain of redox centers consisting of FAD, [2Fe-2S], and [4Fe-4S]. Although the electrons from the [3Fe-4S] cluster can be transferred either to heme *b* or ubiquinone, ubiquinone is preferable (10, 11). It has been shown that the heme *b* is neither an absolute structural requirement nor essential for quinone reduction (23, 24). In addition, once the heme *b* is reduced, it can also in turn reduce ubiquinone (10, 11). Therefore, the heme *b* is proposed to serve as an electron sink in the electron transfer pathway (25, 26). In this process, quinone likely receives the first electron from the [3Fe-4S] cluster to form the semiquinone, and then, the semiquinone radical is stabilized by rapid electron equilibration between the heme *b* and ubiquinone (26, 27). Finally, the semiquinone accepts a second electron to complete full reduction, which is transported from either the heme *b* or the [3Fe-4S] cluster. Given the overall structural features and arrangement of redox centers between human CII and the SQRs from *E. coli* (10) and *S. scrofa* (11) (*SI Appendix*, Fig. S4), they likely have a very similar electron transfer pathway. Based on these structural similarities, we propose that the human CII succinate- and ubiquinone-binding sites are likely to be connected by a similar chain of redox centers that include FAD, [2Fe-2S], [4Fe-4S], [3Fe-4S], and heme *b* (Fig. 3). However, although the structural features and electron transfer pathway of the human CII appear to be similar to that of *E. coli* (10) and *S. scrofa* (11) SQRs, there is some amino acid sequence variability (*SI Appendix*, Fig. S4*B*). Therefore, we have estimated how the sequence variability affects the structure using MD simulations. Considering the high sequence identity between human CII and *S. scrofa* SQR among the available structures of complex II, the potential implication of a slight difference of residue sequence between these two species was investigated (*SI Appendix*, Fig. S6*A*). The MD simulations indicate that the structure of human CII is more conformationally stable than that of the *S. scrofa* SQR (*SI Appendix*, Fig. S6*B*), which may be potentially useful for electron transport.

Human CII Mutations Related with Diseases. Mutants of human CII result in mitochondrial dysfunction. This can manifest in two clinical diseases: either as a primary mitochondrial disease or as susceptibility to tumorigenesis (28). The clinically affected individuals harbor genetic variants within the SDHA (29–34), SDHB (30, 35–40), and SDHD (41, 42) subunits. However, there

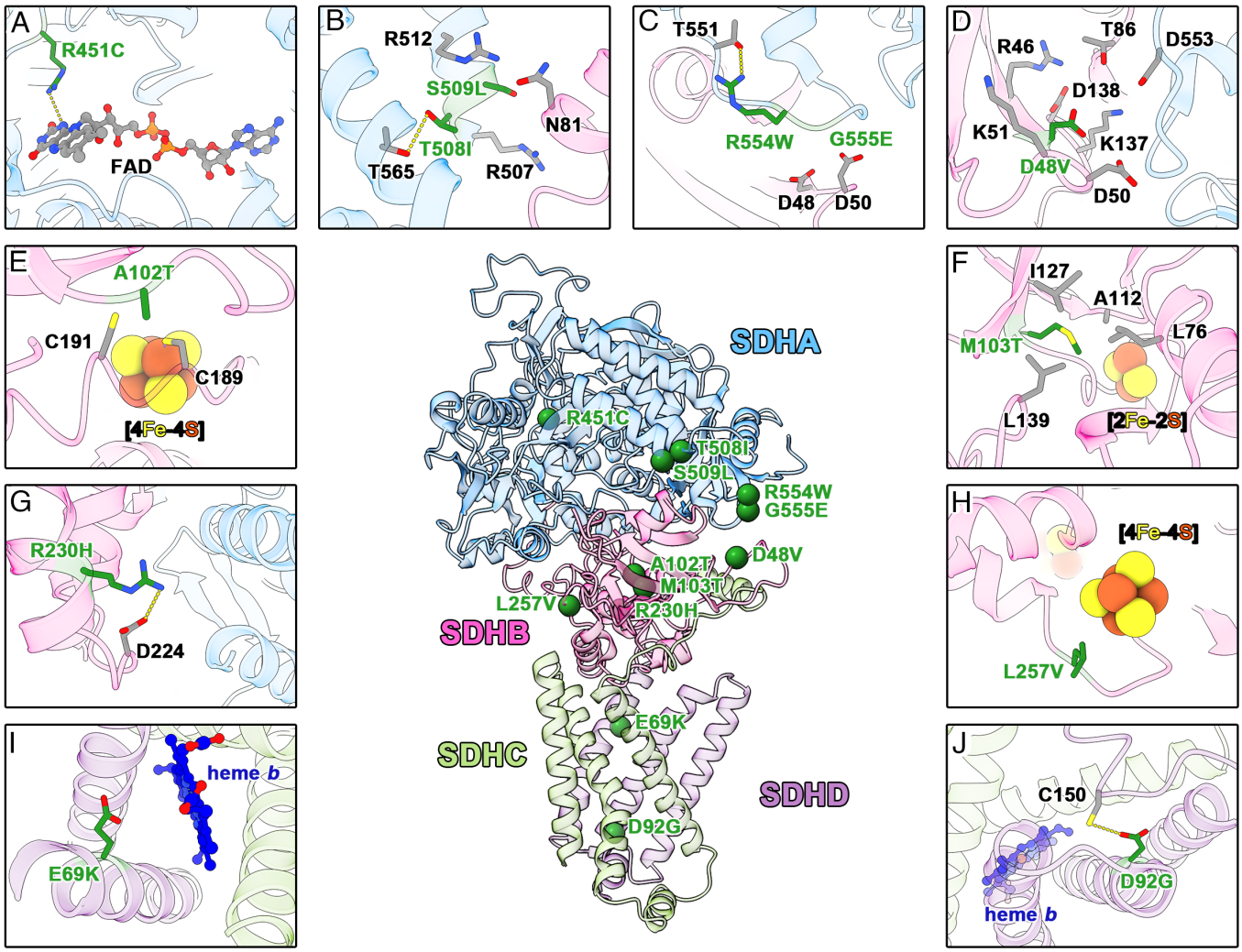

Fig. 4. Location of the ten clinically relevant mutations in human CII. (*A-J*) The mutants are highlighted in green, and the surrounding residues are shown in gray sticks. The central panel shows an overview of the locations of the ten mutations.

are no reports of primary mitochondrial dysfunction involving SDHC variants. Knowledge of the exact location of the mutations is important to explain the molecular basis for a specific disease (Fig. 4). The dominant substitution of Arg451Cys (29) in the subunit SDHA abolishes a hydrogen bond with the FAD cofactor (Fig. 4*A*), thus potentially affecting FAD binding. The Thr508Ile and Ser509Leu mutants in SDHA have been reported in one individual (30). These mutations are situated at the SDHA–SDHB interface (Fig. 4*B*) and result in the loss of hydrogen-bonding interactions with neighboring polar residues and are therefore purported to affect heterodimer formation. Arg554 and Gly555 within a helical domain of SDHA are also situated at the SDHA–SDHB interface. The Arg554Trp (31) mutation abrogates a hydrogen bond with Thr551 within SDHA (Fig. 4*C*). The Gly555Glu (32–34) replacement creates a negative charge at an external loop of SDHA (Fig. 4*C*). This change may impact the folding of this segment and assembly with SDHB. The Asp48Val substitution in SDHB is the change that is most frequently reported in clinical studies (30, 35–38). Substitution of a negatively charged aspartate with an uncharged valine introduces a hydrophobic residue into a hydrophilic region between the SDHA–SDHB interface, reducing the stability of this contact (Fig. 4*D*). The substitution of Ala102Thr (39) results in the formation of new polar bonds with Cys189, and Cys191 within the SDHB subunit (Fig. 4*E*), possibly altering the local tertiary structure around the [4Fe-4S] cluster. Interestingly, an adjacent variant, Met103Thr of SDHB, is also reported in a case of mitochondrial disease (36). Met103 is located proximal to the [2Fe-2S] cluster, and its substitution with threonine may influence the structure of surrounding hydrophobic region (Fig. 4*F*). The Arg230His variant of SDHB is associated with both mitochondrial complex II deficiency and susceptibility to tumorigenesis growth (38, 40). This substitution removes a salt bridge with Asp224 in the SDHB subunit (Fig. 4*G*). The Leu257Val (38) substitution in SDHB alters the interaction with the [4Fe-4S] cluster (Fig. 4*H*), and the Glu69Lys (41) change in SDHD will affect interactions with heme *b* (Fig. 4*I*). These two mutations may induce the change in the orientation of the [4Fe-4S] cluster and heme *b*, respectively, and affect the capacity for electron transfer. The Asp92Gly (42) substitution removes a hydrogen-bonding interaction with the residue Cys150 (Fig. 4*J*), which may affect the stability of transmembrane helices of the SDHD subunit on the intermembrane space side. In summary, these substitutions tend to occur in regions of the proteins that result in instability of the complex, leading to a functional deterioration of the complex. However, more studies are needed to reveal the exact interactions between these substitutions and the relevant disease states. In addition, as for the human mutations, they could generally be mapped on the available homologous structures from different organisms. It is remarkable, however, that human CII does not have 100% amino acid sequence identity with any of the available structures of complex II (*SI Appendix*, Figs. S4*B*, S6*A* and S7). This suggests that the mutations of human CII do not always accurately map on the existing structures. Hence, the current structure can directly reflect the potential impacts that result from the mutations of human CII. Overall, this structure improves our understanding of the molecular basis for human CII mutation-related disease and lays the foundation for the development of rational treatments for these diseases.

Materials and Methods

Cloning and Expression of Protein. The gene for SDHD was amplified from human cDNA by PCR and cloned into the pQCXIP vector with a 3× Flag tag inserted at the C terminus of SDHD. The primer sequences are listed in *SI Appendix*, Table S5. 293F cells were transfected with the reconstructed plasmid using polyethylenimine (PEI, Polysciences) and then were subjected to 5 μg/mL puromycin (Sangon Biotech) for 2 wk. The cells were cultivated in SMM 293-TII medium (Sino Biological), harvested at a density of 5×10^6 cells/mL, and collected and rinsed in PBS buffer. Cell pellets were stored at −80 °C for future use.

Isolation of Human Mitochondria. The cell pellets were resuspended in ice-cold buffer consisting of 20 mM 3-(N-morpholino)propanesulfonic acid (MOPS), pH 7.4, 250 mM sucrose, and 1 mM EGTA and incubated for 10 min. The suspension was homogenized (40 mL buffer/300 mL pellets) with 20 strokes of a Dounce tissue grinder (Kimble). Cell debris was removed by centrifugation at 1,000 ×g for 10 min at 4 °C. The supernatant was collected and centrifuged (10,000 × g, 4 °C, 10 min) again to isolate the mitochondria. Finally, the pellets were collected as mitochondrial fractions.

Purification and Identification of the Respiratory Complex II. To purify complex II, mitochondria were resuspended in buffer containing 20 mM MOPS (pH 7.4), 100 mM NaCl, and 1% (w/v) lauryl maltose neopentyl glycol (LMNG, Anatrace) and incubated for about 30 min with rotation at 4 °C. The lysate was then centrifuged at 40,000 × g for 40 min at 4 °C and incubated with Anti – DYKDDDDK G1 Affinity Resin (GenScript) at 4 °C for 1 h. The beads were washed with 10 column volumes (CVs) of washing buffer containing 20 mM MOPS (pH 7.4), 100 mM NaCl, and 0.004% (w/v) LMNG. Then, protein was eluted with 5 CV elution buffer containing 20 mM MOPS (pH 7.4), 100 mM NaCl, and 0.02% (w/v) glyco-diosgenin (GDN, Anatrace) supplemented with 0.2 mg/mL 1× Flag peptides (GenScript). Finally, complex II was concentrated and loaded onto a Superose 6 Increase 10/300 size-exclusion column (GE Healthcare) equilibrated with elution buffer. Peak fractions containing protein were collected and concentrated for protein gel electrophoresis analysis, MS analysis, and electron microscopy studies.

To identify the cofactors in the protein sample, low-temperature electron paramagnetic resonance (EPR) spectrum was acquired using a Bruker X-band (9.4 GHz) EMX plus 10/12 spectrometer equipped with an Oxford Instruments ESR 910 continuous helium flow cryostat. A cylindrical resonator (ER4119hs TE011) was used for EPR data collection. The sample was placed into quartz EPR tubes (Wilmad, 707-SQ-250 M, 3 mm i.d., 4 mm o.d.) for measurements. The temperature was set at 10 K. Other experimental conditions were as follows: microwave power, 0.2 mW; modulation amplitude, 5 Gauss; modulation frequency, 100 kHz; and resonance frequency, ~9.404 GHz. For each sample, multiple scans were accumulated to obtain a good S/N ratio.

Kinetics of Enzyme Activity Assay. The succinate-quinone oxidoreductase enzymatic activity of human CII was determined by performing a succinate-2,6-dichlorophenolindophenol (DCIP, Sigma) assay in the presence of ubiquinone-1 (UQ1, Sigma) as previously described (43). UQ1 was used as the intermediate electron acceptor to examine succinate dehydrogenase activity. The final reaction mixture contained elution buffer, human complex II (2.29 μg), 0.00625 to 0.8 mM sodium succinate (Sigma), 0.5 mM UQ1, and 200 μM DCIP. Reactions were initiated by addition of succinate, and the absorbance change at 600 nm was monitored over time. All assays were performed at 25 °C by using the Cytation5 imaging reader (BioTek). All the enzymatic experiments were repeated three times, and data were processed with GraphPad Prism 6.

Electron Microscopy Sample Preparation and Imaging. First, 3 μL of 2.9 mg/mL human CII was applied to H_2/O_2 glow-discharged 300-mesh Quantifoil R 1.2/1.3 grids (Quantifoil, Micro Tools GmbH) and subsequently blotted using an FEI Vitrobot and then frozen in liquid ethane. Then, the grids were imaged on a Thermo Fisher Krios G4 microscope (Thermo Fisher Scientific) equipped with a cold field emission gun, a Selectris X energy filter, and a Falcon 4 detector. The energy filter was operated with a slit width of 10 e^-V to remove inelastically scattered electrons. Image stacks were collected using EPU software at a pixel size of 0.73 Å/pixel with a total dose of 50 $e^-/Å^2$.

Imaging Processing. A total of 6,700 image stacks were subjected to beam-induced motion correction and CTF estimation using CryoSPARC (44). A total of 1,788,861 particles were picked automatically and were extracted with a box size of 384 pixels. After several rounds of 2D and 3D classifications, 322,768 particles were used to perform ab initio reconstruction and heterogeneous refinement. Afterward, the candidate model and 114,967 particles were selected and refined using NU refinement to generate the final cryo-EM map at a 2.86 Å resolution.

Local resolution ranges were also analyzed within CryoSPARC according to the gold standard Fourier shell correlation (FSC) cutoff of 0.143 (45). All dataset processing is shown in *SI Appendix*, Fig. S2.

Model Building and Refinement. The atomic model of complex II was built based on the structure of SDHA/B/C/D predicted from the AlphaFold Protein Structure Database (46). To start model building, the predicted domains of four subunits were docked into the EM density map by using Chimera (47), followed by manual adjustment of main chains and side chains in Coot (48) and real space refinement in PHENIX (49).

Figure Images. The majority of the images presented in the figures were created using UCSF Chimera X (50).

Simulation System Construction. The structures of wild-type and mutant human CII were processed on the H++ website (http://newbiophysics.cs.vt.edu/H++/) to analyze the protonation state of ionizable groups in the protein at pH 7.0. Next, the protein/membrane system solvated in water was built using PACKMOL-Memgen software, an automated workflow for building the lipid bilayer of the membrane protein. Here, the POPC (1-palmitoyl-2-oleoyl-sn-glycero-3-phosphocholine) lipid bilayer with dimensions 90 × 90 × 158 Å was applied to embed the transmembrane region of human CII, while the cytoplasmic domain of human CII was exposed to solvents. Na^+ and Cl^- ions at a physiological concentration of 0.15 M were added to neutralize the system. The force fields ffSB19 and LIPID17 were applied to parameterize the standard amino acids and lipids, respectively, and a TIP3P model was chosen for water parameterization. The parameter files of HEME molecule were downloaded from the AMBER parameter database (http://amber.manchester.ac.uk/) maintained by Richard Bryce. All parameters of the iron–sulfate clusters, i.e., SF4, F3S, and FES, referred to Marcel Swart's study (51). The parameters of FAD and UQ molecules were both generated using the Antechamber tool, while their electrostatic charges were computed based on the RESP (restrained electrostatic potential) methodology. The PE molecule was constructed as a nonstandard lipid molecule, and its parameters were derived from the lipid force field LIPID17. With the above parameters, the leap tool in the AMBER package was used to generate the molecular topology and coordinate files for simulation.

Molecular Dynamics Simulation. Molecular dynamic simulation was performed using AMBER 2020 (52). Before dynamic simulation, 5,000 steps of energy minimization with a force constant of 10 kcal/mol $Å^2$ and 2.5 kcal/mol $Å^2$ on protein and lipids, respectively, were performed on waters to remove potential steric clashes between the solute and solvents. Then, two stages of equilibrium simulations were carried out to relax the protein and lipid molecules by gradually decreasing the restraint force. The first one includes three short simulations with a constant volume and temperature (NVT) ensemble. Lipids were restrained with a force field of 2.5 kcal/mol $Å^2$, while the restraint force on protein was decreased from 10.0 to 1.0 kcal/mol $Å^2$. A time step of 1 fs was set to maintain simulation stability. The second run used three short simulations in total 1.5 ns to completely relax the whole system with an extremely low force. At this stage, constant pressure and temperature (NPT) was applied to the simulation. The time step was increased to 2 fs, while the SHAKE algorithm was used to fix high-frequency hydrogen motions (53). Subsequently, a 10-ns NPT simulation without any restraints was performed to further equilibrate the system. Langevin dynamics was used to control the temperature at 303.15 K in NVT and NPT simulations (54). In the NPT simulations, additional semi-isotropic pressure coupling and constant surface tension were applied to the simulation of lipid bilayers (55). After the equilibrium simulation, a 50 ns of production simulation was carried out to generate the trajectory for the final structure analysis. Coordinates were printed every 100 ps so that in total, 500 frames were contained in the final trajectory. The CPPTRAJ module in AMBER was applied to analyze the trajectory (56). The rmsd of protein backbone atoms was used to measure the overall conformational stability of the structure. It was calculated as the positional difference of all backbone atoms between the frames produced during the simulation and compared with the starting conformation. We used the definition that the smaller the deviation, the more stable was the protein structure.

Data, Materials, and Software Availability. EM map and atomic coordinates have been deposited in the Electron Microscopy Data Bank (EMDB; https://www.ebi.ac.uk/pdbe/emdb) and Protein Data Bank (PDB; http://www.rcsb.org), respectively, under the following ID codes: EMD-34225 (57) and PDB 8GS8 (58) for the human respiratory complex II.

ACKNOWLEDGMENTS. We would like to thank the Bio-Electron Microscopy Facility of ShanghaiTech University and the Advanced Bioimaging Technology Platform of Guangzhou Laboratory. We also would like to thank the Steady High Magnetic Field Facilities, High Magnetic Field Laboratory, Chinese Academy of Sciences. We would be grateful to Dr Min Zhou and Ms Mei Li for their help in collecting EM images. This work was supported by grants from the National Key Research and Development Program of China (Grant No. 2022YFA1305900 to H.G.), and the National Natural Science Foundation of China (Grant Nos. 32100976 and 82222042 to H.G.).

1. M. Saraste, Oxidative phosphorylation at the fin de siècle. *Science* **283**, 1488–1493 (1999).
2. I. Vercellino, L. A. Sazanov, The assembly, regulation and function of the mitochondrial respiratory chain. *Nat. Rev. Mol. Cell Biol.* **23**, 141–161 (2022).
3. B. Moosavi, E. A. Berry, X.-L. Zhu, W.-C. Yang, G.-F. Yang, The assembly of succinate dehydrogenase: A key enzyme in bioenergetics. *Cell. Mol. Life Sci.* **76**, 4023–4042 (2019).
4. J. B. Spinelli *et al.*, Fumarate is a terminal electron acceptor in the mammalian electron transport chain. *Science* **374**, 1227–1237 (2021).
5. R. K. Aggarwal *et al.*, Functional succinate dehydrogenase deficiency is a common adverse feature of clear cell renal cancer. *Proc. Natl. Acad. Sci. U. S. A.* **118**, e2106947118 (2021).
6. K. A. Andrews *et al.*, Tumour risks and genotype–phenotype correlations associated with germline variants in succinate dehydrogenase subunit genes SDHB, SDHC and SDHD. *J. Med. Genet.* **55**, 384–394 (2018).
7. M. J. Farshbaf, A. Kiani-Esfahani, Succinate dehydrogenase: Prospect for neurodegenerative diseases. *Mitochondrion* **42**, 77–83 (2018).
8. C. R. D. Lancaster, A. Kröger, M. Auer, H. Michel, Structure of fumarate reductase from *Wolinella* succinogenes at 2.2 Å resolution. *Nature* **402**, 377–385 (1999).
9. T. M. Iverson, C. Luna-Chavez, L. R. Croal, G. Cecchini, D. C. Rees, Crystallographic studies of the *Escherichia coli* quinol-fumarate reductase with inhibitors bound to the quinol-binding site. *J. Biol. Chem.* **277**, 16124–16130 (2002).
10. V. Yankovskaya *et al.*, Architecture of succinate dehydrogenase and reactive oxygen species generation. *Science* **299**, 700–704 (2003).
11. F. Sun *et al.*, Crystal structure of mitochondrial respiratory membrane protein complex II. *Cell* **121**, 1043–1057 (2005).
12. L. Huang *et al.*, 3-nitropropionic acid is a suicide inhibitor of mitochondrial respiration that, upon oxidation by complex II, forms a covalent adduct with a catalytic base arginine in the active site of the enzyme. *J. Biol. Chem.* **281**, 5965–5972 (2006).
13. H. Shimizu *et al.*, Crystal structure of mitochondrial quinol–fumarate reductase from the parasitic nematode Ascaris suum. *J. Biochem.* **151**, 589–592 (2012).
14. H. Gong *et al.*, Cryo-EM structure of trimeric *Mycobacterium smegmatis* succinate dehydrogenase with a membrane-anchor SdhF. *Nat. Commun.* **11**, 1–8 (2020).
15. X. Zhou *et al.*, Architecture of the mycobacterial succinate dehydrogenase with a membrane-embedded Rieske FeS cluster. *Proc. Natl. Acad. Sci. U.S.A.* **118**, e2022308118 (2021).
16. J. R. Bolla, M. T. Agasid, S. Mehmood, C. V. Robinson, Membrane protein–lipid interactions probed using mass spectrometry. *Annu. Rev. Biochem.* **88**, 85–111 (2019).
17. C. Martens *et al.*, Direct protein-lipid interactions shape the conformational landscape of secondary transporters. *Nat. Commun.* **9**, 1–12 (2018).
18. S. Mehmood *et al.*, Structural and functional basis for lipid synergy on the activity of the antibacterial peptide ABC transporter McjD. *J. Biol. Chem.* **291**, 21656–21668 (2016).
19. E. Pyle *et al.*, Structural lipids enable the formation of functional oligomers of the eukaryotic purine symporter UapA. *Cell. Chem. Biol.* **25**, 840–848.e4 (2018).
20. K. Gupta *et al.*, The role of interfacial lipids in stabilizing membrane protein oligomers. *Nature* **541**, 421–424 (2017).
21. A. M. Hoffnagle, V. H. Eng, U. Markel, F. A. Tezcan, Computationally guided redesign of a heme-free cytochrome with native-like structure and stability. *Biochemistry* **61**, 2063–2072 (2022).
22. C. C. Page, C. C. Moser, X. Chen, P. L. Dutton, Natural engineering principles of electron tunnelling in biological oxidation–reduction. *Nature* **402**, 47–52 (1999).
23. E. Maklashina, R. A. Rothery, J. H. Weiner, G. Cecchini, Retention of heme in axial ligand mutants of succinate-ubiquinone oxidoreductase (complex II) from *Escherichia coli*. *J. Biol. Chem.* **276**, 18968–18976 (2001).
24. C. R. T. Vibat, G. Cecchini, K. Nakamura, K. Kita, R. B. Gennis, Localization of histidine residues responsible for heme axial ligation in cytochrome *b556* of complex II (succinate: ubiquinone oxidoreductase) in *Escherichia coli*. *Biochemistry* **37**, 4148–4159 (1998).
25. R. Horsefield *et al.*, Structural and computational analysis of the quinone-binding site of complex II (succinate-ubiquinone oxidoreductase): A mechanism of electron transfer and proton conduction during ubiquinone reduction. *J. Biol. Chem.* **281**, 7309–7316 (2006).
26. Q. M. Tran, R. A. Rothery, E. Maklashina, G. Cecchini, J. H. Weiner, The quinone binding site in *Escherichia coli* succinate dehydrogenase is required for electron transfer to the heme b^*. *J. Biol. Chem.* **281**, 32310–32317 (2006).
27. R. F. Anderson, R. Hille, S. S. Shinde, G. Cecchini, Electron transfer within complex II: Succinate: Ubiquinone oxidoreductase of *Escherichia coli*. *J. Biol Chem.* **280**, 33331–33337 (2005).
28. M. Fullerton, R. McFarland, R. W. Taylor, C. L. Alston, The genetic basis of isolated mitochondrial complex II deficiency. *Mol. Genet. Metab.* **131**, 53–65 (2020).
29. C. Courage *et al.*, SDHA mutation with dominant transmission results in complex II deficiency with ocular, cardiac, and neurologic involvement. *Am. J. Med. Genet. A.* **173**, 225–230 (2017).
30. C. L. Alston *et al.*, Recessive germline SDHA and SDHB mutations causing leukodystrophy and isolated mitochondrial complex II deficiency. *J. Med. Genet.* **49**, 569–577 (2012).
31. T. Bourgeron *et al.*, Mutation of a nuclear succinate dehydrogenase gene results in mitochondrial respiratory chain deficiency. *Nat. Genet.* **11**, 144–149 (1995).

32. A. Levitas *et al.*, Familial neonatal isolated cardiomyopathy caused by a mutation in the flavoprotein subunit of succinate dehydrogenase. *Eur. J. Hum. Genet.* **18**, 1160–1165 (2010).
33. A. T. Pagnamenta *et al.*, Phenotypic variability of mitochondrial disease caused by a nuclear mutation in complex II. *Mol. Genet. Metab.* **89**, 214–221 (2006).
34. R. V. Coster *et al.*, Homozygous Gly555Glu mutation in the nuclear-encoded 70 kDa flavoprotein gene causes instability of the respiratory chain complex II. *Am. J. Med. Genet A.* **120**, 13–18 (2003).
35. A. Ardissone *et al.*, Mitochondrial leukoencephalopathy and complex II deficiency associated with a recessive SDHB mutation with reduced penetrance. *Mol. Genet. Metab. Rep.* **5**, 51–54 (2015).
36. G. Helman *et al.*, Magnetic resonance imaging spectrum of succinate dehydrogenase–related infantile leukoencephalopathy. *Ann. Neurol.* **79**, 379–386 (2016).
37. A. Vanderver *et al.*, Whole exome sequencing in patients with white matter abnormalities. *Ann. Neurol.* **79**, 1031–1037 (2016).
38. S. Grønborg *et al.*, Leukoencephalopathy due to complex II deficiency and Bi-allelic SDHB mutations: Further cases and implications for genetic counselling. *JIMD Rep.* **33**, 69–77 (2016).
39. P. Kaur, S. Sharma, R. Kadavigere, K. M. Girisha, A. Shukla, Novel variant p. (Ala102Thr) in SDHB causes mitochondrial complex II deficiency: Case report and review of the literature. *Ann. Hum. Genet.* **84**, 345–351 (2020).
40. N. Burnichon *et al.*, The succinate dehydrogenase genetic testing in a large prospective series of patients with paragangliomas. *J. Clin. Endocrinol. Metab.* **94**, 2817–2827 (2009).
41. C. B. Jackson *et al.*, Mutations in SDHD lead to autosomal recessive encephalomyopathy and isolated mitochondrial complex II deficiency. *J. Med. Genet.* **51**, 170–175 (2014).
42. C. L. Alston *et al.*, A recessive homozygous p.Asp92Gly SDHD mutation causes prenatal cardiomyopathy and a severe mitochondrial complex II deficiency. *Hum. Genet.* **134**, 869–879 (2015).
43. K. Hards, S. M. Rodriguez, C. Cairns, G. M. Cook, Alternate quinone coupling in a new class of succinate dehydrogenase may potentiate mycobacterial respiratory control. *FEBS Lett.* **593**, 475–486 (2019).
44. A. Punjani, J. L. Rubinstein, D. J. Fleet, M. A. Brubaker, cryoSPARC: Algorithms for rapid unsupervised cryo-EM structure determination. *Nat. Methods* **14**, 290–296 (2017).
45. N. Grigorieff, Frealign: An exploratory tool for single-particle cryo-EM. *Methods Enzymol.* **579**, 191–226 (2016).
46. J. Jumper *et al.*, Highly accurate protein structure prediction with AlphaFold. *Nature* **596**, 583–589 (2021).
47. E. F. Pettersen *et al.*, UCSF Chimera–a visualization system for exploratory research and analysis. *J. Comput. Chem.* **25**, 1605–1612 (2004).
48. P. Emsley, B. Lohkamp, W. G. Scott, K. Cowtan, Features and development of Coot. *Acta Crystallogr D Biol. Crystallogr.* **66**, 486–501 (2010).
49. P. D. Adams *et al.*, PHENIX: A comprehensive Python-based system for macromolecular structure solution. *Acta Crystallogr. D Biol. Crystallogr.* **66**, 213–221 (2010).
50. E. F. Pettersen *et al.*, UCSF ChimeraX: Structure visualization for researchers, educators, and developers. *Protein Sci.* **30**, 70–82 (2021).
51. A. T. Carvalho, M. Swart, Electronic structure investigation and parametrization of biologically relevant iron–sulfur clusters. *J. Chem. information Modeling* **54**, 613–620 (2014).
52. D. A. Case *et al.*, The Amber biomolecular simulation programs. *J. Comput. Chem.* **26**, 1668–1688 (2005).
53. A. G. Bailey, C. P. Lowe, MILCH SHAKE: An efficient method for constraint dynamics applied to alkanes. *J. Comput. Chem.* **30**, 2485–2493 (2009).
54. N. Grønbech-Jensen, O. Farago, Constant pressure and temperature discrete-time Langevin molecular dynamics. *J. Chem. Phys.* **141**, 194108 (2014).
55. S. V. Bennun, A. N. Dickey, C. Xing, R. Faller, Simulations of biomembranes and water: Important technical aspects. *Fluid Phase Equilib.* **261**, 18–25 (2007).
56. D. R. Roe, T. E. Cheatham III, PTRAJ and CPPTRAJ: Software for processing and analysis of molecular dynamics trajectory data. *J. Chem. Theory Comput.* **9**, 3084–3095 (2013).
57. Z. Du *et al.*, Cryo-EM structure of the human respiratory complex II. Electron Microscopy Data Bank. https://www.ebi.ac.uk/emdb/EMD-34225. Deposited 5 September 2022.
58. Z. Du *et al.*, Cryo-EM structure of the human respiratory complex II. Protein Data Bank. https://www.rcsb.org/structure/8GS8. Deposited 5 September 2022.